Journal of Organometallic Chemistry 894 (2019) 28–38

Contents lists available at ScienceDirect

Journal of Organometallic Chemistry

journal homepage: www.elsevier.com/locate/jorganchem

Axial ligand mediated switchable rotary motions in a ferrocene-bridged diiron(III) porphyrin dimer

Anjani Kumar Pandey, Sarnali Sanfui, Firoz Shah Tuglak Khan, Sankar Prasad Rath*

Department of Chemistry, Indian Institute of Technology Kanpur, Kanpur, 208016, India

ARTICLE INFO

Article history:
Received 14 February 2019
Received in revised form
12 April 2019
Accepted 1 May 2019
Available online 8 May 2019

Dedicated to Professor V. Chandrasekhar on the occasion of his 60th birthday.

Keywords:
Electronic structure
Ferrocene
Rotatory motion
Fe(III) porphyrin
Axial coordination
Structure elucidation

ABSTRACT

In the present work, we have utilized ferrocene-bridged diiron(III) porphyrin dimer and investigate the rotary motions mediated by axial ligands exploiting conformational flexibility of the ferrocene linker. Diiron(III) porphyrin dimer can switch easily between the *syn* and *anti* rotamers reversibly based on the axial coordination and thereby forming complexes with different structure and properties for the development of synthetic molecular machines. While the five-coordinate diiron(III) complex with chloride axial ligand and its μ-oxo dimer are in *syn*-conformation, their six-coordinate complexes are stabilized in *anti*-conformation. All the complexes are isolated in the solid state and five-coordinate complexes are also structurally characterized. Spectroscopic investigation through UV–visible spectra, solid-state Mössbauer, EPR, and ^{1}H NMR studies confirm the presence of high and low-spin diiron(III) porphyrins, respectively, for five and six-coordinate complexes.

1. Introduction

The nanometer-scale molecular machines are vital for the functioning of biological systems and are accountable for all biochemical processes starting from the generation of high-energy molecule adenosine triphosphate (ATP) to the muscular expansions and contractions for controlled motion [1]. Taking inspiration from such biomolecular systems, synthetic chemists have progressively designed more complex switchable nanoscale artificial molecular machines. Majority of such developed systems are based on sophisticated and synthetically challenging mechanically interlocked architectures (MIAs) [2]. These MIAs have been well utilized to engineer a number of molecular machines among which synthetic rotary motors have been quite well-known [3].

The rotational motion represents one of the most important mechanical processes engaged in the conversion of energy at various levels ranging from mammalian cell ATP synthases, rotary motions of large protein chains, to a variety of macroscopic motors having fundamental implications for mankind [4]. Therefore, the primary objective has been controlling such rotational motion involving organic/inorganic frameworks [3,4]. A well-studied molecular rotor has been ferrocene, which is an 18 electron sandwich organometallic complex consisting of a Fe(II) ion between two freely rotating cyclopentadiene (Cp) rings. The free rotation of the Cp rings is mediated by the sandwiched Fe(II) ion which acts as an “atomic ball-bearing”. Subsequently, a controlled *anti* and *syn* conformational switching can be well achieved in 1,1′-disubstituted ferrocenes [5]. Ferrocene derivatives have been attractive building units for designing of non-interlocked synthetic molecular machines owing to their molecular ball-bearing and reversible electrochemical properties [5,6]. In the present work, we have utilized ferrocene bridged porphyrin dimer and investigate the rotary motions mediated by axial ligands to form different structure and properties just by exploiting conformational flexibility of the ferrocene linker. A reasonable choice of the linker in porphyrin dimer also allows a precise control over the spatial orientation of the porphyrin rings which mediates inter-ring interactions and possible electronic communications [7–9].

---

* Corresponding author.
E-mail address: sprath@iitk.ac.in (S.P. Rath).

https://doi.org/10.1016/j.jorganchem.2019.05.002

2. Experimental section

2.1. Materials

The synthesis of free base ferrocene-bridged porphyrin dimer, 1,1′-Bis{5,10,15-trisphenyl-20-phen-4′-ylporphyrin}ferrocene dicarboxylate abbreviated as H_4FcTPP, was done following a known procedure [10]. Reagents and solvents were purchased from commercial sources and were purified by standard protocols before use.

2.1.1. Synthesis of **1**·Cl_2

100 mg (0.067 mmol) of H_4FcTPP, was dissolved in 100 mL tetrahydrofuran. Excess ferrous chloride (84.9 mg, 0.670 mmol) was added to the solution and the whole mixture was refluxed for 2.5 h under N_2 atmosphere. The reaction mixture was cooled and transferred to a separating funnel. 150 mL dichloromethane was added and washed with 0.2 N HCl. The organic layer was then separated and dried over anhydrous sodium sulphate. Resulting solution was dried completely and purified by column chromatography. The major fraction, eluted with dichloromethane, was collected and dried under vacuum. The brown solid, thus obtained, was dissolved in a minimum volume of chloroform and layered with hexane. After 5–6 days in air at room temperature, a dark crystalline solid was obtained which was then collected by filtration, washed well with mother liquor, and then dried under vacuum. Yield: 88 mg (78%). ESI-MS: *m/z* 1642.2541 ($[\mathbf{1}\cdot Cl_2{-}Cl]^+$). UV–vis (dichloromethane) [λ_{max}, nm (ε, $M^{-1}\,cm^{-1}$)]: 418 (2.6×10^5), 497 (2.5×10^2), 553 (6.4×10^2), 636 (2.2×10^1). ^1H NMR ($CDCl_3$, 295 K): Pyrr-*H*, 82.7; Phenyl-*H*, 13.8, 14.2, 14.4, 15.0, 15.2; Fc-*H*, 5.5, 4.7 ppm. EPR data: in CH_2Cl_2 (120 K), $g_\perp = 5.94$ and $g_\parallel = 1.99$.

2.1.2. Synthesis of **2**

70 mg of $\mathbf{1}\cdot Cl_2$ (0.041 mmol) was dissolved in 50 mL dichloromethane. 50 mL of 5% NaOH solution was added to it and resulting solution was stirred for 20 min at room temperature. The reaction mixture was then transferred to a separating funnel; the organic layer was separated and dried over anhydrous sodium sulphate. The resulting solution was completely dried under reduced pressure and purified by column chromatography using basic alumina. The major fraction, eluted with dichloromethane, was collected and vacuum dried to obtain green solid. The solid thus obtained was dissolved in a minimum volume of chloroform and layered with cyclohexane. After 3–4 days in air at room temperature, a dark crystalline solid was obtained which was then collected by filtration, well washed with mother liquor, and then dried under vacuum. Yield: 60 mg (90%). UV–vis (dichloromethane) [λ_{max}, nm (ε, $M^{-1}\,cm^{-1}$)]: 409 (2.4×10^5), 514 (2.6×10^2), 580 (6.8×10^2), 610 (2.3×10^1). ^1H NMR ($CDCl_3$, 295 K): Pyrr-*H*, 13.5; Phenyl-*H*, 7.7, 7.6, 7.5, 7.4, 7.3; Fc-*H*, 5.4, 4.6 ppm.

Complexes $[\mathbf{1}\cdot(L)_4]Cl_2$ were prepared using a general procedure; details are given for $[\mathbf{1}\cdot(Im)_4]Cl_2$ as a representative case.

2.1.3. Synthesis of [**1**·$(Im)_4$]Cl_2

$\mathbf{1}\cdot Cl_2$ (70 mg, 0.041 mmol) was dissolved in 10 mL of dichloromethane and 17 mg (0.240 mmol) of imidazole was added to it. The mixture was then stirred for 10 min. The resulting solution was filtered to remove any solid residue, evaporated to dryness, washed well with hexane and was vacuum dried. Yield: 65 mg (82%). ESI-MS: *m/z* 939.7380 ($[\mathbf{1}\cdot(Im)_4]^{2+}$). UV–vis (dichloromethane) [λ_{max}, nm (ε, $M^{-1}\,cm^{-1}$)]: 416 (2.7×10^5), 512 (2.4×10^2), 570 (6.1×10^2), 612 (2.5×10^1). Conductivity (CH_2Cl_2, 10^{-4} M solution at 295 K): $\Lambda_M = 42\,\Omega^{-1}\,cm^2\,mol^{-1}$.$^1H$ NMR ($CDCl_3$, 295 K): Pyrr-*H*, −18.8, −18.4, −17.8, −17.2; Phenyl-*H*, 10.0; Imidazole-NH_c, 11.1, Imidazole-H_a, -9.9; Fc-*H*, 7.5 ppm. EPR data: in CH_2Cl_2 (120 K), $g_1 = 2.87$, $g_2 = 2.28$, $g_3 = 1.56$.

2.1.4. [**1**·(4-MeIm)$_4$]Cl_2

Yield: 64 mg (83%). ESI-MS: *m/z* 967.7520 ($[\mathbf{1}\cdot(4\text{-}MeIm)_4]^{2+}$). UV–vis (dichloromethane) [λ_{max}, nm (ε, $M^{-1}\,cm^{-1}$)]: 419 (2.6×10^5), 515 (2.4×10^2), 569 (5.6×10^2), 610 (2.1×10^1). Conductivity (CH_2Cl_2, 10^{-4} M solution at 295 K): $\Lambda_M = 41\,\Omega^{-1}\,cm^2\,mol^{-1}$.$^1H$ NMR ($CDCl_3$, 295 K): ^1H NMR ($CDCl_3$, 295 K): Pyrr-*H*, −17.5, −16.9, −16.4(2); Phenyl-*H*, 12.1; Imidazole-NH_c, 11.8, Imidazole-H_a, −15.0, Imidazole-4Me_b, 14.7; Fc-*H*, 8.0 ppm. EPR data: in CH_2Cl_2 (120 K), $g_1 = 2.85$, $g_2 = 2.26$, $g_3 = 1.59$.

2.1.5. [**1**·(1-MeIm)$_4$]Cl_2

Yield: 62 mg (80%). ESI-MS: *m/z* 967.7416 ($[\mathbf{1}\cdot(1\text{-}MeIm)_4]^{2+}$). UV–vis (dichloromethane) [λ_{max}, nm (ε, $M^{-1}\,cm^{-1}$)]: 417 (2.5×10^5), 511 (2.0×10^2), 598 (5.9×10^2), 651 (1.9×10^1). Conductivity (CH_2Cl_2, 10^{-4} M solution at 295 K): $\Lambda_M = 40\,\Omega^{-1}\,cm^2\,mol^{-1}$.$^1H$ NMR ($CDCl_3$, 295 K): ^1H NMR ($CDCl_3$, 295 K): Pyrr-*H*, −17.7, −17.5, −17.0(2); Phenyl-*H*, 13.8; Imidazole-NMe_c, 17.0, Imidazole-H_a, −7.6; Fc-*H*, 7.9 ppm. EPR data: in CH_2Cl_2 (120 K), $g_1 = 2.88$, $g_2 = 2.24$, $g_3 = 1.55$.

2.1.6. [**1**·(2-MeIm)$_4$]Cl_2

Yield: 63 mg (81%). ESI-MS: *m/z* 967.7533 ($[\mathbf{1}\cdot(2\text{-}MeIm)_4]^{2+}$). UV–vis (dichloromethane) [λ_{max}, nm (ε, $M^{-1}\,cm^{-1}$)]: 417 (2.4×10^5), 530 (2.2×10^2), 580 (6.2×10^2), 640 (2.6×10^1). Conductivity (CH_2Cl_2, 10^{-4} M solution at 295 K): $\Lambda_M = 40\,\Omega^{-1}\,cm^2\,mol^{-1}$.$^1H$ NMR ($CDCl_3$, 295 K): ^1H NMR ($CDCl_3$, 295 K): Pyrr-*H*, −14.6, −14.2, −13.5, −13.3; Phenyl-*H*, 12.9; Imidazole-NH_c, 14.4; Fc-*H*, 7.7 ppm.

2.2. Instrumentation

UV–vis spectral measurements were performed on a PerkinElmer UV/Vis spectrometer. Electron paramagnetic resonance (EPR) spectra were obtained on a Bruker EMX EPR spectrometer and simulated using EasySpin software [11]. ^{57}Fe Mössbauer spectra were measured using a Wissel 1200 spectrometer and a proportional counter. The radioactive source used was ^{57}Co(Rh) in a constant acceleration mode. Isomer shifts (δ) were calculated relative to α-iron foil at the room temperature. The ESI mass spectra were recorded with a Waters Micromass QuattroMicro triple quadrupole mass spectrometer. Proton NMR spectra were recorded on a JEOL 500 MHz instrument over a 100 kHz bandwidth with 64 K data points and a 5 ms 90° pulse. For a typical spectrum, between 2000 and 3000 transients were accumulated with a delay time of 50 µs. The residual proton resonances of the solvent were used as a secondary reference. Cyclic voltammetric measurements were done using a BAS Epsilon electrochemical workstation in CH_2Cl_2 with 0.1 M tetra(*n*-butyl)ammonium hexafluorophosphate ($TBAPF_6$) as supporting electrolyte with reference electrode Ag/AgCl and platinum wire as auxiliary electrode. The concentrations of the compounds were in the order of 10^{-3} M. Under the same experimental conditions, the ferrocene/ferrocenium redox couple was obtained at $E_{1/2} = +0.45$ (65) V versus Ag/AgCl.

2.3. X-ray structure solution and refinement

Crystals were coated with light hydrocarbon oil and mounted in the 100 K dinitrogen stream of Bruker SMART APEX CCD diffractometer equipped with a low-temperature CRYO Industries apparatus and intensity data were collected using graphite-monochromated MoKα radiation having $\lambda = 0.71073$ Å. The data integration and reduction were processed through SAINT software [12]. The absorption correction was also applied [13]. All the structures were solved employing the direct method with SHELXS-97 and were refined on F^2 by full-matrix least-squares technique

Table 1
Crystal data and data collection parameters.

	$1\cdot Cl_2$	**2**
Formula	$C_{100}H_{62}Cl_2Fe_3N_8O_4$	$C_{100}H_{62}Fe_3N_8O_5$
T, K	100(2)	100(2)
Formula weight	1678.02	1623.12
Crystal system	Triclinic	Triclinic
Space group	P −1	P −1
a, Å	14.6040(8)	10.0841(6)
b, Å	15.9666(8)	17.9657(10)
c, Å	23.9559(13)	23.1950(13)
α, deg	73.7480(10)	87.192(2)
β, deg	76.6100(10)	89.452(2)
γ, deg	64.3950(10)	78.160(2)
V, Å^3	4796.4(4)	4107.8(4)
Radiation (λ, Å)	Mo Kα (0.71073)	Mo Kα (0.71073)
Z	2	2
d_{calcd}, g.cm^{-3}	1.162	1.312
$F(000)$	1724	1672
Crystal size(mm^3)	0.18 × 0.14 x 0.10	0.16 × 0.12 x 0.10
μ, mm^{-1}	0.555	0.583
No. of unique data	17567	15263
No. of parameters refined	1054	1003
GOF on F^2	1.033	1.024
$R1^{a}$ $[I>2\sigma(I)]$	0.1020	0.0968
$wR2^{a}$ (all data)	0.2833	0.2669
Largest diff. peak and hole	0.611 and −0.570 e.Å^{-3}	1.710 and −0.762 e.Å^{-3}

$$^{a}R1 = \frac{\sum|F_o| - |F_c|}{\sum|F_o|};\ ^{b}wR2 = \sqrt{\frac{\sum\left[w\left(F_o^2 - F_c^2\right)^2\right]}{\sum\left[w\left(F_o^2\right)^2\right]}}$$

using SHELXL-2018 program package [14]. Non-hydrogen atoms beside a phenyl group of **2** were refined in an anisotropic manner. Hydrogens were treated as riding atoms in the refinement using SHELXL default parameters. Crystal data and data collection parameters for the complexes are mentioned in Table 1.

2.4. Computational details

Molecular modeling was carried out with a B3LYP hybrid functional using the Gaussian 09, revision B.01, software package [15]. The method employed was Becke's three parameter hybrid exchange functional with the nonlocal correlation provided by the Lee, Yang, and Parr expression, and Vosko, Wilk, and Nuair 1980 correlation functional (III) for local correction [16]. The basis set was 6−31G** for carbon, nitrogen, oxygen, chlorine and hydrogen atoms and LANL2DZ for iron atom. The coordinate were taken directly from the single crystal X-ray data and subsequently unconstrained geometry optimization of the molecule was done keeping in the high-spin state for $\mathbf{1}\cdot Cl_2$ and low-spin state for $[\mathbf{1}\cdot(1\text{-MeIm})_4]Cl_2$. In all the calculations, the Self-Consistent Reaction Field (SCRF) method was adopted for the inclusion of solvent correction using chloroform as solvent. No imaginary frequencies were obtained in the frequency calculations of the optimized geometries. Energies, containing zero-point corrections at 298.15 K and 1 atm, were taken from the Gaussian frequency calculation. The diagrams of the optimized geometries as well as molecular orbitals were made through Chemcraft software [17].

3. Results and discussion

Ferrocene-bridged porphyrin dimer (H_4FcTPP, **1**) was synthesized following a reported procedure [10]. Iron metal insertion was done by refluxing the free base ligand H_4FcTPP in tetrahydrofuran with excess $FeCl_2$ under inert atmosphere for 2.5 h. The resulting solution was purified by column chromatography in silica gel using dichloromethane as eluent to form complex $\mathbf{1}\cdot Cl_2$. Upon treatment of 5% NaOH solution with dichloromethane solution of $\mathbf{1}\cdot Cl_2$, an immediate color change from red to green was observed due to the formation of μ-oxo diiron(III) porphyrin dimer, **2** (Fig. 1). Addition of 5% HCl solution converts μ-oxo diiron(III) porphyrin dimer, **2** immediately into $\mathbf{1}\cdot Cl_2$. X-ray structures of **2** and $\mathbf{1}\cdot Cl_2$ have been reported here.

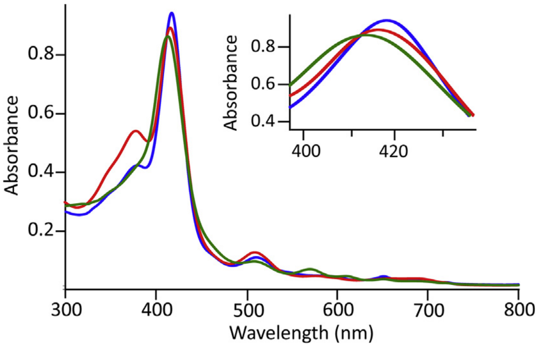

Fig. 1. UV−visible spectra (in dichloromethane at 295 K) of $\mathbf{1}\cdot Cl_2$ (red line), $[\mathbf{1}\cdot(4\text{-MeIm})_4]Cl_2$ (blue line), and **2** (green line). (For interpretation of the references to color in this figure legend, the reader is referred to the Web version of this article.)

Ferrocene-bridged porphyrin dimer can switch easily between the *syn* and *anti* rotamers (Fig. 2) based on the nature of axial coordination. Upon addition of axial ligand L into the dichloromethane solution of $\mathbf{1}\cdot Cl_2$, several hexa-coordinated complexes $[\mathbf{1}\cdot(L)_4]Cl_2$ are synthesized which are isolated and spectroscopically characterized (Scheme 1). The axial ligands (L) used in the present investigations are 2-methylimidazole (2-MeIm), imidazole (Im), 4-methylimidazole (4-MeIm), and 1-methylimidazole (1-MeIm). A change is the UV−visible spectra has observed during the axial coordination by L into $\mathbf{1}\cdot Cl_2$. For example, the Soret band at 416 nm for $\mathbf{1}\cdot Cl_2$ undergoes a bathochromic shift to 419 nm in $[\mathbf{1}\cdot(4\text{-MeIm})_4]Cl_2$ (Fig. 1). Similar UV−vis spectral changes are also observed for other six-coordinated complexes in the series (Table 2). Dichloromethane solutions of $[\mathbf{1}\cdot(L)_4]Cl_2$, upon treatment with 5% NaOH, produce the oxo-bridged dimer **2**. The synthetic outline and the list of the complexes are shown in Scheme 1 along with their abbreviations. X-ray structures of $\mathbf{1}\cdot Cl_2$ and **2** have been

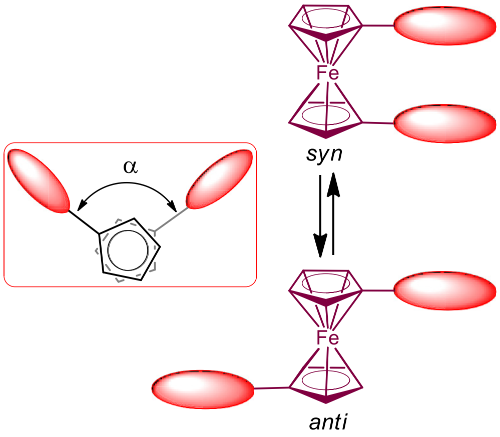

Fig. 2. Schematic representation of two rotamers of Ferrocene: *anti* (rotation angle, α = 180°) and *syn* (α = 0°).

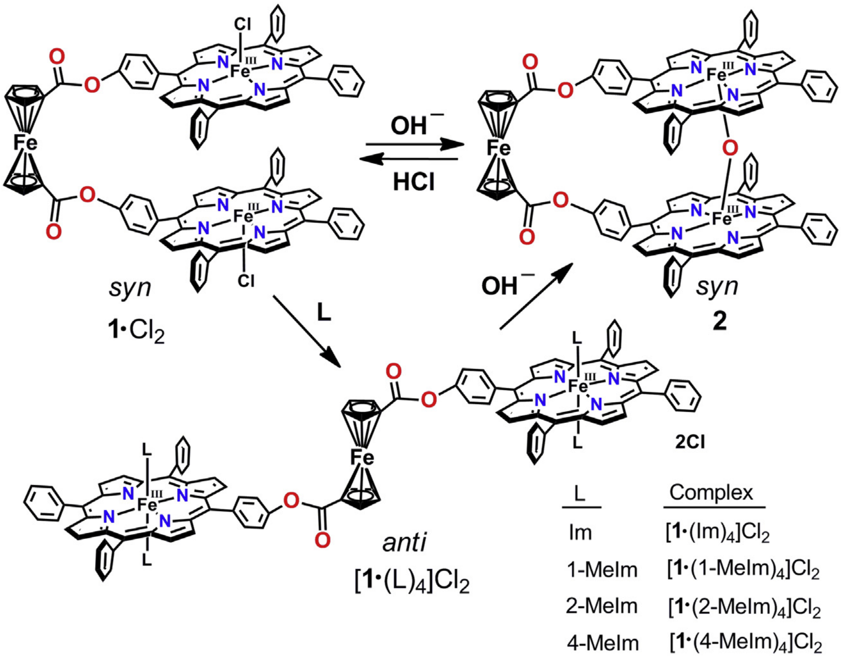

Scheme 1. The synthetic outline and the list of the complexes are shown along with their abbreviations.

Table 2
UV–visible spectral data (in dichloromethane at 295 K) of the complexes.

Complexes	UV–vis spectra (nm)	
	Soret band	Other bands
1·Cl_2	416	497, 553, 636
2	409	514, 580, 610
[**1**·$(Im)_4]Cl_2$	418	512, 570, 612
[**1**·$(1\text{-}MeIm)_4]Cl_2$	417	511, 598, 651
[**1**·$(2\text{-}MeIm)_4]Cl_2$	417	530, 580, 640
[**1**·$(4\text{-}MeIm)_4]Cl_2$	419	515, 569, 610

grown successfully and are reported here. However, in spite of several attempts, single crystals suitable for X-ray structure determination could not be produced for [**1**·$(L)_4]Cl_2$, however, the complexes have been characterized by a large number of spectroscopic techniques which includes ESI-MS, ^1H NMR and EPR studies. Fig. 3 displays ESI-MS spectra of **1**·Cl_2 and [**1**·$(1\text{-}MeIm)_4]Cl_2$ which revealed desired signals at *m/z* 1642.2541 and 967.7416 assigned for $[\mathbf{1}\text{-}Cl_2{-}Cl]^+$ and $[\mathbf{1}\cdot(1\text{-}MeIm)_4]^{2+}$, respectively (Fig. 3). The isotopic distribution patterns of the experimental mass are also in good agreements with the calculated patterns which further confirm the formation of the complexes. ESI-MS spectra of other complexes have also been shown in Figs. S1–S3. The molar conductance values for the six-coordinate complexes [**1**·$(Im)_4]Cl_2$, [**1**·$(1\text{-}MeIm)_4]Cl_2$, [**1**·$(2\text{-}MeIm)_4]Cl_2$ and [**1**·$(4\text{-}MeIm)_4]Cl_2$ are found to be 42, 40, 40 and 41 Ω^{-1} cm^2 mol^{-1}, respectively, at 295 K which are similar to the values observed for 1:2 electrolytes in dichloromethane solution [18].

3.1. Crystallographic characterization

Dark brown crystals of **1**·Cl_2, and **2** were obtained *via* slow diffusion of *n*-hexane and cyclohexane, respectively, into the chloroform solutions of the respective complexes at room temperature in air. Both the complexes crystallize in the triclinic crystal system having P-1 space group. Molecular structures of the complexes are displayed in Figs. 4–7 along with their packing diagrams. The crystal data and data collection parameters are given in Table 1. Numbering scheme for the atoms is displayed in Chart 1. Selected distances and angles are listed in Table 3 while the selected structural and geometrical parameters are listed in Table 4. As seen from Table 3, the average Fe–Npor and Fe-Cl distances are, respectively, 2.058(6) and 2.236(2) in **1**·Cl_2, while the iron atom is displaced by 0.51 Å from the least-square plane of $C_{20}N_4$ porphyrinato core ($\Delta^{Fe}{}_{24}$). For **2**, the Fe–Npor and Fe-O distances are 2.080(5) Å and 1.757(4) Å, respectively, while $\Delta^{Fe}{}_{24}$ is 0.51 Å in the complex. Fe–Npor and $\Delta^{Fe}{}_{24}$ distances for both the complexes are very characteristic of high-spin ($S = 5/2$) iron(III) porphyrins [19–23]. The most striking feature of the structure in **2** is almost a linear Fe-O-Fe unit with an angle of 179.3(3)°. Two intramolecular porphyrin rings are on the top of each other and oriented in nearly eclipsed conformation in **2** while the rings are twisted along the ferrocene bridge in **1**·Cl_2 (Figs. 4 and 5).

The conformational variations in the ferrocene-bridged porphyrin dimer can be well understood from Table 4. The free-base H_4FcTPP has a rotation angle (α) of 17.4° and lateral shift of 5.13 Å while upon diiron μ-oxo formation, the two porphyrin rings are on top of each other and move closer to each other forming nearly eclipsed conformation with a rotation angle (α) of 14.0° and lateral shift of 0.27 Å only. A rotation angle (α) of 16.18° and the lateral shift of 5.33 Å have also been observed for **1**·Cl_2. It is interesting to note here that, two six-coordinate iron(III)porphyrin cores in [**1**·$(L)_4]Cl_2$ are in *anti*-conformation (*vide infra*). This indeed demonstrates the ability of ferrocene moiety to rotate around the central iron to form a large variety of complexes which is triggered by axial coordination.

3.2. Mössbauer spectroscopy

Mössbauer spectroscopy is one of the most important tools for iron spin state elucidation in iron(III) porphyrin complexes [19–23]. The spectra of the crystalline samples of **1**·Cl_2 and **2** were recorded at 100 K in zero magnetic field and are displayed in Fig. 8.

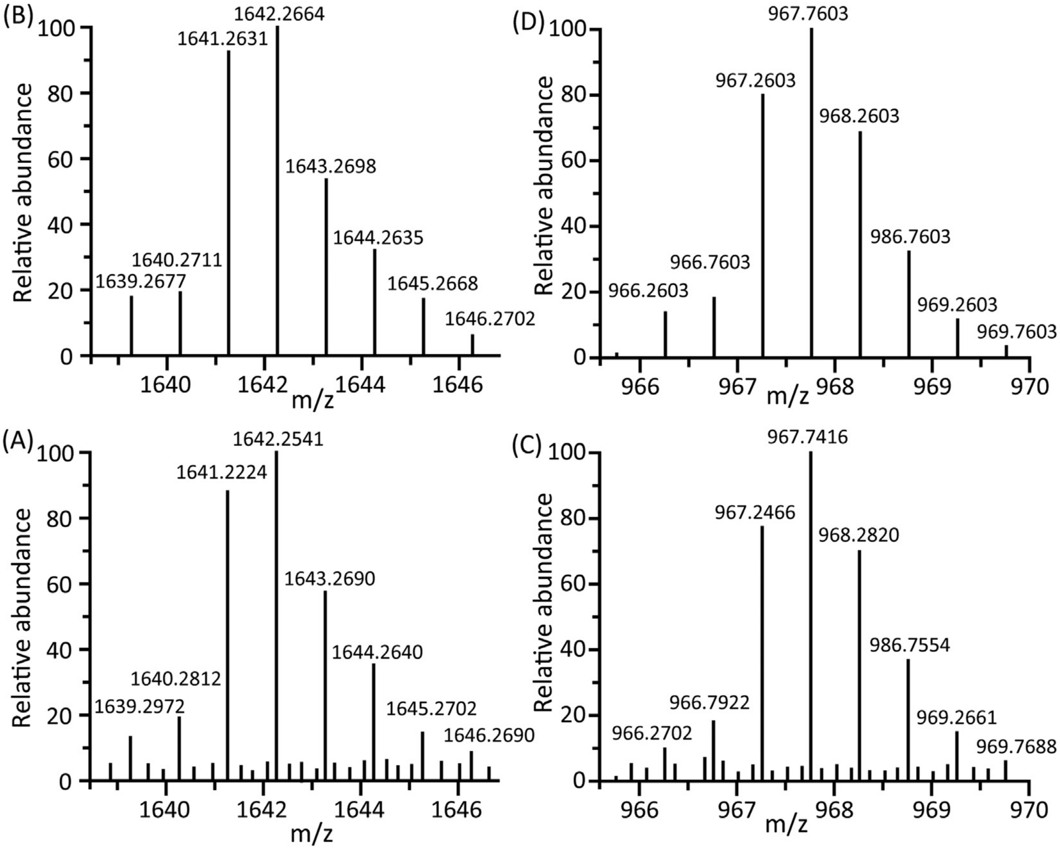

Fig. 3. Isotopic distribution patterns of ESI-MS spectra of (A) experimental and (B) simulated of $1\cdot Cl_2$ and (C) experimental and (D) simulated ESI-MS spectra of $[1\cdot(1\text{-MeIm})_4]Cl_2$.

Both the complexes $\mathbf{1}\cdot Cl_2$ and **2** display two doublets marking the presence of two different iron centers within the molecule. A small quadrupole splitting δ (ΔEq) = 0.38 (0.67) mms^{-1} for $\mathbf{1}\cdot Cl_2$ and δ (ΔEq) = 0.31 (0.63) mms^{-1} for **2** is observed which is characteristic of high-spin ($S = 5/2$) state of iron in the complexes [7,8]. The other doublet observed with large quadrupole splitting δ (ΔEq) = 0.43 (2.27) mms^{-1} for $\mathbf{1}\cdot Cl_2$ and δ (ΔEq) = 0.44 (2.27) mms^{-1} for **2** is very characteristic of low-spin iron(II) of the ferrocene linker.

3.3. EPR spectroscopy

The EPR spectral measurements have been carried out for $\mathbf{1}\cdot Cl_2$, $[\mathbf{1}\cdot(Im)_4]Cl_2$, $[\mathbf{1}\cdot(1\text{-MeIm})_4]Cl_2$ and $[\mathbf{1}\cdot(4\text{-MeIm})_4]Cl_2$ complexes at 120 K for both solid as well as in solution phase and the spectra are shown in Fig. 9. For $\mathbf{1}\cdot Cl_2$ the spectra is axially symmetric with $g_\perp = 5.94$ and $g_\parallel = 1.99$ in dichloromethane at 120 K. Similar g values are obtained also in the solid phase. These results provide unequivocal evidence of high-spin ($S = 5/2$) nature of Fe(III) of complex $\mathbf{1}\cdot Cl_2$ both in solid and solution. The X-band EPR spectra of $[\mathbf{1}\cdot(L)_4]Cl_2$ display rhombic-type spectral features both in solution as well as solid phases. The g values obtained upon simulations are, $g_3 = 1.55$, $g_2 = 2.24$ and $g_1 = 2.88$ for $[\mathbf{1}\cdot(1\text{-MeIm})_4]Cl_2$; $g_3 = 1.59$, $g_2 = 2.26$ and $g_1 = 2.85$ for $[\mathbf{1}\cdot(4\text{-MeIm})_4]Cl_2$ and $g_3 = 1.56$, $g_2 = 2.28$ and $g_1 = 2.87$ for $[\mathbf{1}\cdot(Im)_4]Cl_2$. The spectral patterns are very characteristics of six-coordinate low-spin ($S = 1/2$) iron(III) porphyrins having bis-imidazole ligation [9a,b,25-27].

A qualitative representation of the splitting pattern of d-orbitals observed for low-spin iron(III) d^5 complexes is shown in Fig. 10. As compared to the splitting within lower and higher energy d orbital subsets, the crystal field splitting is much larger between the two highest and three lowest energy d orbitals. In case of iron(III) porphyrin systems, the tetragonal distortion occurs because of the lower crystal field of porphyrin macrocycle than that of the axially coordinated imidazoles. Such tetragonal splitting pattern arises because of the perpendicular orientation of the axial ligands where the d_{xz} and d_{yz} orbitals (d_π set) are degenerate. Moreover, the presence of an unpaired electron in d_π set results into an unstable situation of the complex due to Jahn-Teller effect [27]. When the d_{xz} and d_{yz} orbitals no longer remain degenerate, it introduces a rhombic distortion which arises when both the planar axial ligands are relatively parallel in orientation [27]. Therefore, a rhombic splitting patters is comparatively much stable in terms of energy as compared to the octahedral or tetragonal splitting. However, when both the planar axial ligands are almost in perpendicular orientation, a ‘large g_{max}’ EPR signal is observed. In this case, $(dxy)^2(dxz,dyz)^3$ is the electronic ground state in which the dxz and dyz orbitals are almost degenerate and the splitting between them is usually less than the value of the spin-orbit coupling constant, λ [27].

The relative orientations of planar axial ligand have been a matter of interest for quite some time in bis-imidzole coordinated ferriheme systems [25,27]. The perpendicular orientations of the planar axial ligands are triggered by highly distorted porphyrin macrocycles [27]. From theoretical calculations, it has been observed that both the rings in $[\mathbf{1}\cdot(L)_4]Cl_2$ are somehow distorted and the axial ligands are relatively oriented in perpendicular fashion (*vide infra*). Despite such perpendicular orientation of axial ligands, a rhombic type EPR spectra is observed for $[\mathbf{1}\cdot(L)_4]Cl_2$ which suggest a decrease in overall symmetry due to the presence

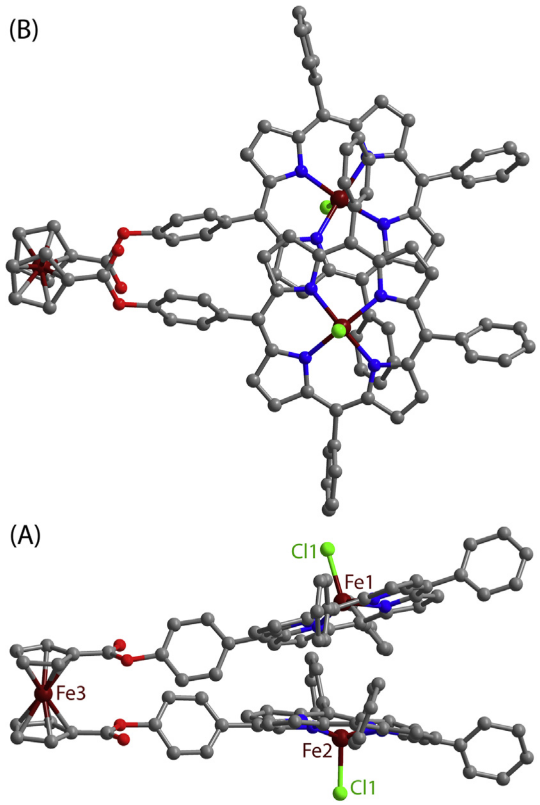

Fig. 4. (A) Side and (B) top views of molecular structure of **1**$\cdot$Cl$_2$ at 100 K (H-atoms have been omitted for clarity).

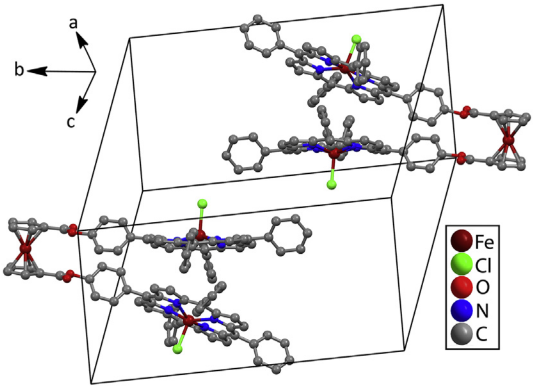

Fig. 5. Diagram illustrating the molecular packing of **1**$\cdot$Cl$_2$ (H-atoms have been omitted for clarity).

of intrinsic asymmetry within the porphyrin dimer [9a,b]. Similar observation has also been found for *meso*-hydroxy heme complex where a rhombic type EPR spectrum is observed even though both the axial ligands are perpendicular to each other [28].

3.4. ^{1}H NMR spectroscopy

^{1}H NMR spectroscopy is a very powerful tool to analyze the solution structure and properties of the iron porphyrin complexes [26]. The ^{1}H NMR spectrum of **1**$\cdot$Cl$_2$ is shown in Fig. 11. The β-pyrrole proton signals are downfield shifted to 80 ppm. The σ spin

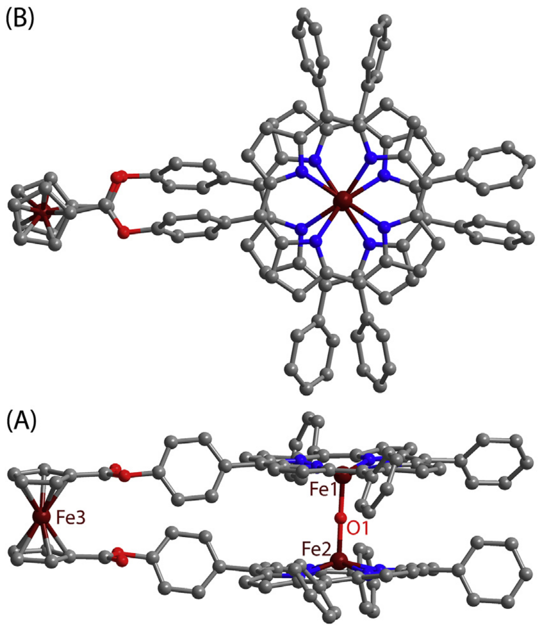

Fig. 6. (A) Side and (B) top views of molecular structure of **2** at 100 K (H-atoms have been omitted for clarity).

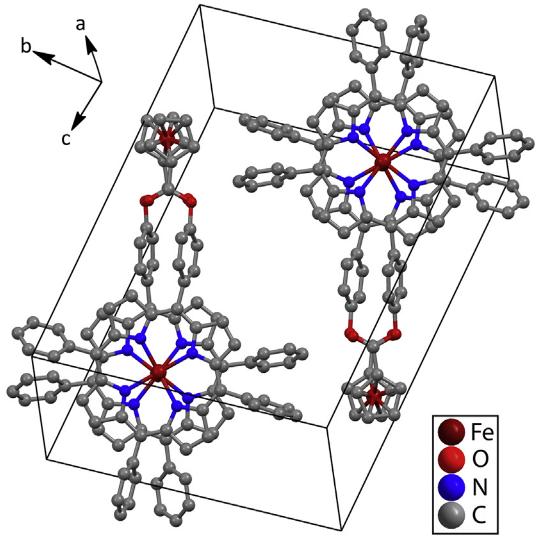

Fig. 7. Diagram illustrating the molecular packing of **2** (H-atoms have been omitted for clarity).

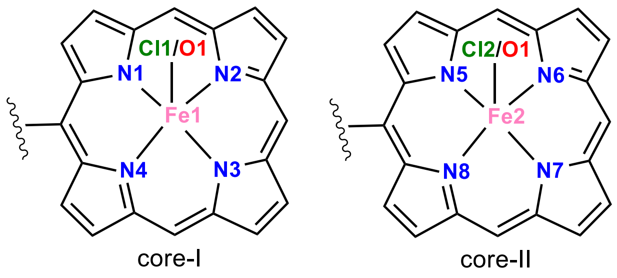

Chart 1. Atom numbering scheme used for the X-ray structures of **1**$\cdot$Cl$_2$ and **2**.

Table 3
Selected distances (Å) and angles (°) for the Fe^{III} complexes.

	$\mathbf{1}\cdot Cl_2$	**2**
Fe1–N1	2.068(6)	2.095(6)
Fe1–N2	2.051(6)	2.088(6)
Fe1–N3	2.045(6)	2.080(5)
Fe1–N4	2.068(6)	2.084(5)
Fe1–O1/Cl1	2.238(2)	1.759(5)
Fe2–N5	2.039(5)	2.080(5)
Fe2–N6	2.052(6)	2.065(6)
Fe2–N7	2.070(6)	2.080(5)
Fe2–N8	2.069(6)	2.079(5)
Fe2-O1-Fe1		179.2(3)
Fe2–O1/Cl2	2.234(2)	1.759(5)
N1–Fe1–N2	87.4(2)	86.7(2)
N1–Fe1–N4	85.8(2)	87.4(2)
N2–Fe1–N4	151.0(2)	153.8(2)
N3–Fe1–N1	155.9(3)	152.8(2)
N3–Fe1–N2	87.3(2)	87.1(2)
N3–Fe1–N4	87.6(2)	86.6(2)
N1–Fe1–O1/Cl1	104.66(19)	101.4(2)
N2–Fe1–O1/Cl1	101.89(18)	105.3(2)
N3–Fe1–O1/Cl1	99.39(18)	105.8(2)
N4–Fe1–O1/Cl1	107.10(18)	100.9(2)
N5–Fe2–N6	88.2(2)	87.9(2)
N5–Fe2–N8	86.1(2)	86.3(2)
N6–Fe2–N8	155.2(2)	152.4(2)
N7–Fe2–N5	152.4(2)	154.8(2)
N7–Fe2–N6	86.4(2)	87.1(2)
N7–Fe2–N8	87.5(2)	86.9(2)
N5–Fe2–O1/Cl2	103.97(19)	104.4(2)
N6–Fe2–O1/Cl2	102.14(19)	101.0(2)
N7–Fe2–O1/Cl2	103.63(18)	100.6(2)
N8–Fe2–O1/Cl2	102.70(17)	106.6(2)

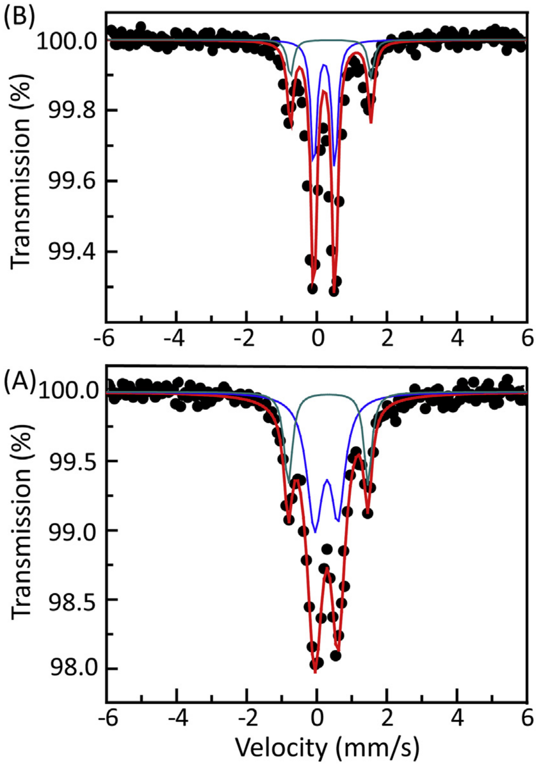

Fig. 8. Mössbauer spectra of crystalline samples of (A) $\mathbf{1}\cdot Cl_2$ and (B) **2** at 100 K.

Table 4
Selected structural and geometrical parameters.

Complex	Fe–Npor[b]	Fe–O/Cl_{ax}[b]	$\Delta^{Fe}{}_{24}$[c]	Δ_{24}[d]	Fe•••Fe[e]	Ct•••Ct[f]	α[g]	θ[h]	Lateral shift[i]
H_4FcTPP[a]	–	–	–	0.04	–	8.99	17.36	29.54	5.13
$\mathbf{1}\cdot Cl_2$	2.058(6)	2.236(2)	0.51	0.10	7.57	6.91	16.18	53.13	5.53
2	2.080(6)	1.757(5)	0.51	0.07	3.51	4.52	14.04	3.62	0.27

[a] Taken from ref 24.
[b] Average value in Å.
[c] Displacement of iron from the mean plane containing $C_{20}N_4$ porphyrinic core in Å.
[d] Average displacement of atoms from the mean plane containing $C_{20}N_4$ porphyrinic core in Å.
[e] Fe•••Fe nonbonding distance between the two porphyrin cores in Å.
[f] Nonbonding distance in Å.
[g] Angle between the two ferrocene “arms” in degree.
[h] Slip angle: average angle (θ) between the vector joining two macrocyclic centers and the unit vectors normal to the two macrocyclic $C_{20}N_4$ porphyrinato cores in degree.
[i] Lateral shift: [sin(θ) x (Ct•••Ct)] in Å.

density transfer mechanism accounts for such large downfield shift of pyrrole proton signals. The protons of the phenyl groups at *meso* positions of the porphyrin macrocycle are also shifted slightly to the downfield region suggesting partial spin density delocalization to the phenyl rings. The spectral shifts are similar to that observed for high-spin ($S = 5/2$) Fe(III)TPP (TPP: 5,10,15,20-tetraphenylporphyrin) complexes known in the literature [26]. Therefore the iron(III) centers in $\mathbf{1}\cdot Cl_2$ are high-spin state. The ^1H NMR spectrum of **2** has also been recorded and is shown in Fig. 11. Because of the strong antiferromagnetic coupling through the oxo bridge between the two high-spin iron(III) centers, the peaks are not downfield shifted except the β-pyrrole protons which appear at $\delta = 13.5$ ppm.

Fig. 12 shows the ^1H NMR spectra of $[\mathbf{1}\cdot(L)_4]Cl_2$ in $CDCl_3$ at 295 K and the inset shows the numbering scheme followed for the imidazole protons. The β-pyrrole signals of $[\mathbf{1}\cdot(Im)_4]Cl_2$ are found to be upfield shifted to $\delta \approx -18$ ppm which is typically observed for low-spin ($S = 1/2$) Fe(III)TPP-type complexes [26]. The other complexes *viz.* $[\mathbf{1}\cdot(4\text{-MeIm})_4]Cl_2$, $[\mathbf{1}\cdot(1\text{-MeIm})_4]Cl_2$ and $[\mathbf{1}\cdot(2\text{-MeIm})_4]Cl_2$ also display the β-pyrrole proton signals near −18 ppm. Due to π-spin delocalization from paramagnetic iron(III) centre to axially coordinated imidazoles, the ^1H NMR signals of imidazoles are shifted to both upfield and downfield regions. To assign the individual proton signals conclusively, several substituted imidazoles have also been used as axial ligands. The observed ^1H NMR spectral pattern of coordinated imidazoles is also similar with previously reported six-coordinate low-spin iron(III) porphyrin dimer [9a,b]. Therefore, the ^1H NMR spectra provide unequivocal evidence of the formation of low-spin six-coordinate iron(III) complex $[\mathbf{1}\cdot(L)_4]Cl_2$ in solution.

3.5. Electrochemical studies

Cyclic voltammetry experiments for $\mathbf{1}\cdot Cl_2$, $[\mathbf{1}\cdot(1\text{-MeIm})_4]Cl_2$ and $[\mathbf{1}\cdot(4\text{-MeIm})_4]Cl_2$ were measured under N_2 in CH_2Cl_2 at 295 K with the supporting electrolyte 0.1 M tetra(*n*-butyl)ammonium

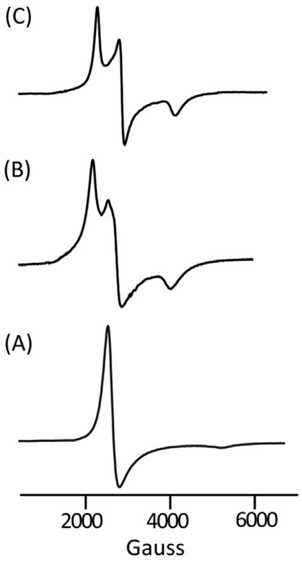

Fig. 9. X-band EPR spectra (in dichloromethane at 120 K) of (A) $\mathbf{1}\cdot Cl_2$, (B) $[\mathbf{1}\cdot(Im)_4]Cl_2$, and (C) $[\mathbf{1}\cdot(4\text{-}MeIm)_4]Cl_2$.

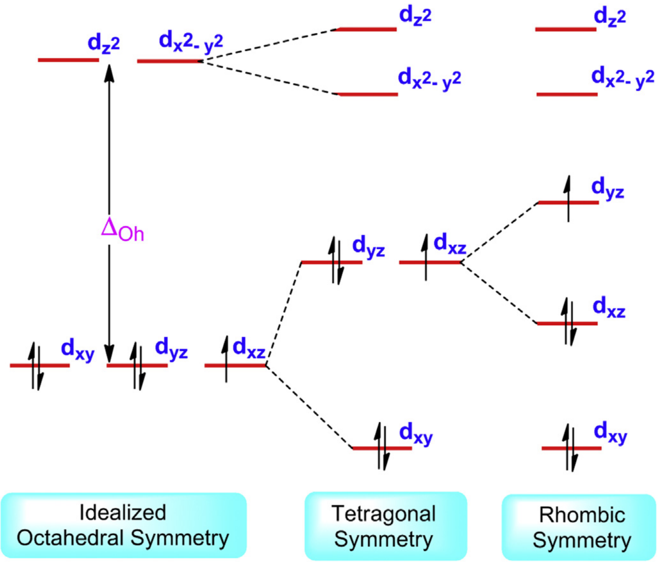

Fig. 10. Splitting pattern of d-orbitals for low-spin iron(III) d^5 systems.

hexafluorophosphate ($TBAPF_6$). Electrochemical data shows that the complexes undergo one three-electron and one two-electron oxidations for the complexes. Fig. 13 shows the cyclic voltammograms for $\mathbf{1}\cdot Cl_2$ and $[\mathbf{1}\cdot(4\text{-}MeIm)_4]Cl_2$ as a representative case. The first three-electron oxidation attribute to the ferrocene/ferrocenium couple that is merged with two 1e-oxidations of porphyrin rings (to form π-cation radicals). This is followed by other 2e-oxidations at a higher positive potential value. Fe^{3+}/Fe^{2+} couple was observed at −0.37 V for $\mathbf{1}\cdot Cl_2$. However, the couple shifted towards more positive for the six-coordinate complex $[\mathbf{1}\cdot(L)_4]Cl_2$; a value of −0.23 and −0.28 V have been observed for L = 1-MeIm and 4-MeIm, respectively. Interestingly, Fe^{III}/Fe^{II} redox couples are observed at −0.36 and −0.37 V, respectively, with 4-MeIm and 1-MeIm axial coordination for ethane-bridged six-coordinate diheme complexes reported earlier [9a].

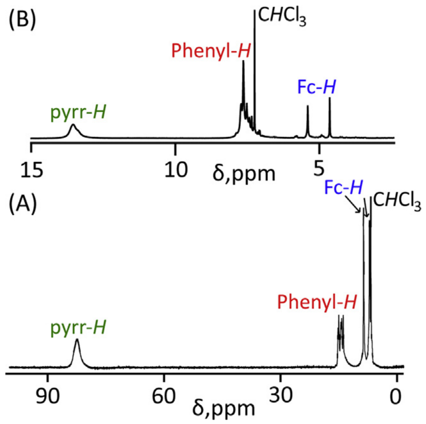

Fig. 11. ^1H NMR spectra (in $CDCl_3$ at 295 K) of (A) $\mathbf{1}\cdot Cl_2$ and (B) **2**.

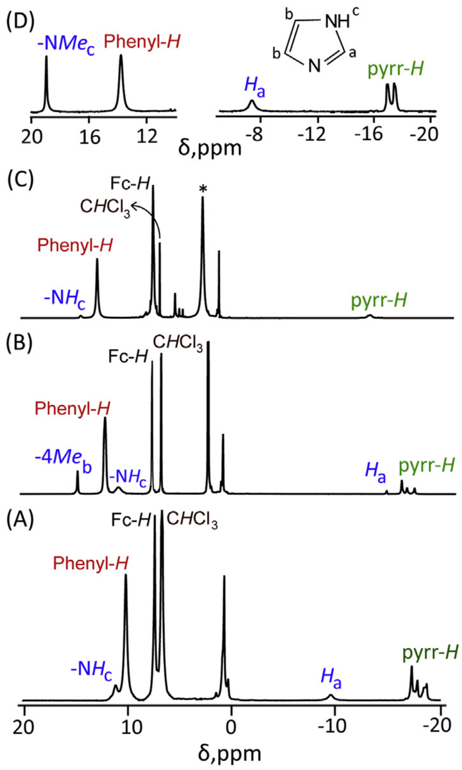

Fig. 12. ^1H NMR spectra (in $CDCl_3$ at 295 K) of (A) $[\mathbf{1}\cdot(Im)_4]Cl_2$, (B) $[\mathbf{1}\cdot(4\text{-}MeIm)_4]Cl_2$, (C) $[\mathbf{1}\cdot(2\text{-}MeIm)_4]Cl_2$, and (D) $[\mathbf{1}\cdot(1\text{-}MeIm)_4]Cl_2$. Peak marked as '*' belongs to signal from free ligand.

3.6. Molecular modeling

DFT calculation has been executed for both five-coordinated high-spin as well as six-coordinated low-spin diiron(III) porphyrin dimers, $\mathbf{1}\cdot Cl_2$ and $[\mathbf{1}\cdot(Im)_4]Cl_2$, respectively. The initial geometry was built by taking the atom coordinates directly from the single crystal X-ray structure of $\mathbf{1}\cdot Cl_2$ which was then optimized keeping both iron(III) centers in high-spin state with an overall spin multiplicty of 11. For $[\mathbf{1}\cdot(Im)_4]Cl_2$, the two chloride counter anions were not included in the calculation giving an overall +2 charge and triplet spin multiciplity to the complex. Subsequently the geometry optimization of $[\mathbf{1}\cdot(Im)_4]^{2+}$ was done; Fig. 14 displays the optimized geometries with selected structural parameters. Both

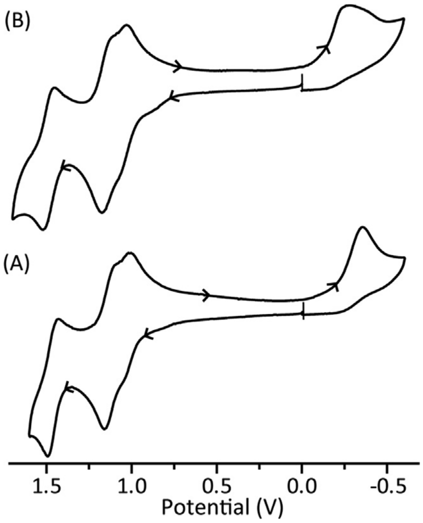

Fig. 13. Cyclic voltammogram (at 295 K) of (A) $\mathbf{1}\cdot Cl_2$, and (B) $[\mathbf{1}\cdot(4\text{-MeIm})_4]Cl_2$ in dichloromethane (scan rate 100 mV/s) with 0.1 M tetra(*n*-butyl)ammonium hexafluorophosphate as supporting electrolyte. The reference electrode was Ag/AgCl.

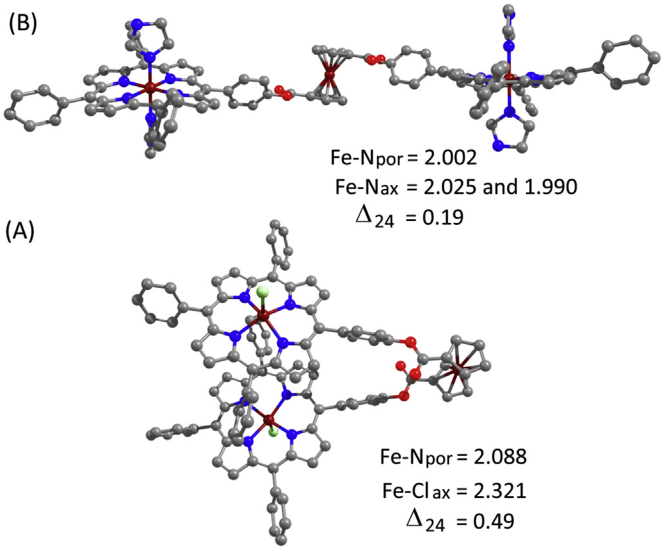

Fig. 14. uB3LYP/6-31G**/LANL2DZ optimized geometries of (A) $\mathbf{1}\cdot Cl_2$ and (B) $[\mathbf{1}\cdot(Im)_4]^{2+}$ with bond distances in Å (hydrogen atoms have been omitted for clarity).

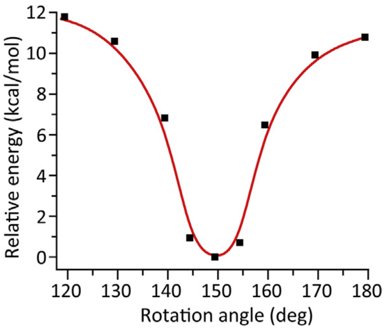

Fig. 15. Plot showing the relative energy (ΔE) upon changing the rotation angle (α) between the two porphyrin cores for $[\mathbf{1}\cdot(Im)_4]^{2+}$.

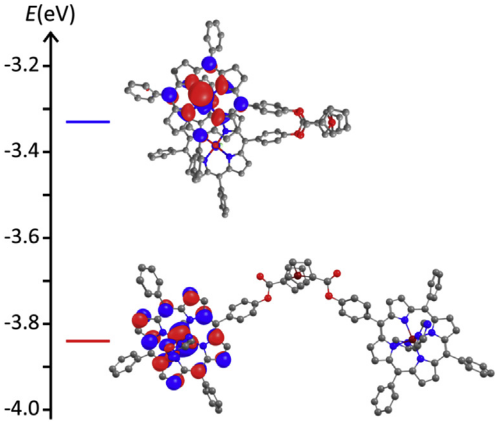

Fig. 16. Plot showing the relative energies of the LUMOs for $\mathbf{1}\cdot Cl_2$ (blue line) and $[\mathbf{1}\cdot(Im)_4]^{2+}$ (red line). (For interpretation of the references to color in this figure legend, the reader is referred to the Web version of this article.)

the porphyrin cores are in *anti* conformation with an angle between both ferrocene "arms" viz. rotation angle (α) of 149°.

To obtain more information into the stabilization of such *anti* conformation of the two porphyrin rings, one dimensional potential energy surface (PES) scan was done on $[\mathbf{1}\cdot(Im)_4]^{2+}$. The rotation angle in the complex was changed in an interval of 5° or 10° in either directions keeping one core fixed in its position and rotating the other one. The relative energies thus calculated of the series of complexes are then plotted against the rotation angle (α) as displayed in Fig. 15. The lowest energy state was found at rotation angle of 149° (as observed in the optimized geometry) and the curve marked more and more destabilization in terms of energy upon changing the rotation angle.

As observed in the electrochemical studies, a positively shifted Fe^{3+}/Fe^{2+} redox potential was observed in case of hexa-coordinate complexes $[\mathbf{1}\cdot(L)_4]Cl_2$ (L = 1-MeIm and 4-MeIm) as compared to five-coordinate $\mathbf{1}\cdot Cl_2$. This was attributed to the change in the iron(III) spin-states on going from high-spin to low-spin. To understand this, the molecular orbitals were analyzed and it was found that the LUMO of $[\mathbf{1}\cdot(Im)_4]^{2+}$ was lower in energy than $\mathbf{1}\cdot Cl_2$ (Fig. 16) which implies that the reduction becomes easier in the former complex than latter. Also, LUMOs were found to have significant coefficients on the metal centers, suggesting metal-cantered reductions in the complexes. Therefore, the Fe^{3+}/Fe^{2+} redox couple is much more positively shifted in $[\mathbf{1}\cdot(L)_4]Cl_2$ (L = 1-MeIm and 4-MeIm) than $\mathbf{1}\cdot Cl_2$ which has also been observed experimentally (*vide supra*).

4. Conclusions

We have utilized here ferrocene-bridged diiron(III) porphyrin dimer and investigate switchable rotary motions mediated by axial ligands exploiting conformational flexibility of the ferrocene linker. While two iron(III) porphyrin units in $\mathbf{1}\cdot Cl_2$ and **2** are in *syn* conformations, their six-coordinate complex $[\mathbf{1}\cdot(L)_4]Cl_2$ (where L: 2-MeIm, Im, 4-MeIm, and 1-MeIm) is stabilized in *anti* conformation. The molecules are isolated in the solid state and the X-ray structures of $\mathbf{1}\cdot Cl_2$ and **2** are reported here. Two intramolecular porphyrin rings are on the top of each other and oriented in nearly eclipsed conformation in **2** while the rings are twisted along the ferrocene bridge in $\mathbf{1}\cdot Cl_2$. The most striking feature of the structure in **2** is almost a linear Fe-O-Fe unit with an angle of 179.3(3)°.

The conformational variations in the ferrocene-bridged porphyrin dimer can be well understood in the complexes. The free-base H_4FcTPP has a rotation angle (α) of 17.4° and lateral shift of 5.13 Å while upon diiron μ-oxo formation, the two porphyrin rings are on top of each other and move closer to form nearly eclipsed conformation with a rotation angle (α) of 14.0° and lateral shift of 0.27 Å only. A rotation angle (α) of 16.18° and the lateral shift of 5.33 Å have also been observed for **1**$\cdot Cl_2$. It is interesting to note here that, two six-coordinate iron(III)porphyrin cores in [**1**$\cdot(L)_4]Cl_2$ are in *anti*-conformation. This indeed demonstrates the ability of ferrocene moiety to rotate around the central iron to form a large variety of complexes reversibly which is triggered by axial coordination. Spectroscopic investigations through UV–visible spectra, solid-state Mössbauer, EPR, and ^{1}H NMR studies confirm the presence of high and low-spin diiron(III) porphyrin centers, respectively, for five and six-coordinate complexes.

Acknowledgment

We are thankful to Science and Engineering Research Board (SERB), India and the Council of Scientific and Industrial Research (CSIR), New Delhi, for financial support. AKP and SS thank CSIR, New Delhi, for their fellowships.

Appendix A. Supplementary data

ESI-MS data (Figs. S1–S3), Cartesian coordinates of the optimized geometries. CCDC 1897280 and 1897281 for **2** and **1**$\cdot Cl_2$, respectively, contain the supplementary crystallographic data for this paper. These data can be obtained free of charge from the Cambridge Crystallographic Data Centre via www.ccdc.cam.ac.uk/data_request/cif.

Supplementary data to this article can be found online at https://doi.org/10.1016/j.jorganchem.2019.05.002.

References

[1] (a) D.A. Leigh, Angew. Chem. Int. Ed. 55 (2016) 14506;
(b) S. Erbas-Cakmak, D.A. Leigh, C.T. McTernan, A.L. Nussbaumer, Chem. Rev. 115 (2015) 10081;
(c) E.R. Kay, D.A. Leigh, Angew. Chem. Int. Ed. 54 (2015) 10080;
(d) J.M. Abendroth, O.S. Bushuyev, P.S. Weiss, C.J. Barrett, ACS Nano 9 (2015) 7746;
(e) M. Schliwa, G. Woehlke, Nature 422 (2003) 759;
(f) G. Karp, Cell and Molecular Biology: Concepts and Experiments, seventh ed., John Wiley and Sons, Inc., Hoboken, NJ, 2013.

[2] (a) G. Barin, R.S. Forgan, J.F. Stoddart, Proc. R. Soc. A 468 (2012) 2849;
(b) C.J. Bruns, J.F. Stoddart, Top. Curr. Chem. 323 (2012) 19;
(c) J.E. Beves, B.A. Blight, C.J. Campbell, D.A. Leigh, R.T. McBurney, Angew. Chem. Int. Ed. 50 (2011) 9260.

[3] (a) J.V. Hernandez, E.R. Kay, D.A. Leigh, Science 306 (2004) 1532;
(b) D.A. Leigh, J.K.Y. Wong, F. Dehez, F. Zerbetto, Nature 424 (2003) 174.

[4] (a) B.S.L. Collins, J.C.M. Kistemaker, E. Otten, B.L. Feringa, Nat. Chem. 8 (2016) 860;
(b) A. Iordache, M. Oltean, A. Milet, F. Thomas, B. Baptiste, E. Saint-Aman, C. Bucher, J. Am. Chem. Soc. 134 (2012) 2653;
(c) G.S. Kottas, L.I. Clarke, D. Horinek, J. Michl, Chem. Rev. 105 (2005) 1281;
(d) S.P. Fletcher, F. Dumur, M.M. Pollard, B.L. Feringa, Science 310 (2005) 80.

[5] (a) S.Ø. Scottwell, J.E. Barnsley, C.J. McAdam, K.C. Gordon, J.D. Crowley, Chem. Commun. 53 (2017) 7628;
(b) S.Ø. Scottwell, J.D. Crowley, Chem. Commun. 52 (2016) 2451;
(c) S.Ø. Scottwell, A.B.S. Elliott, K.J. Shaffer, A. Nafady, C.J. McAdam, K.C. Gordon, J.D. Crowley, Chem. Commun. 51 (2015) 8161;
(d) M. Schmittel, S. De, S. Pramanik, Org. Biomol. Chem. 13 (2015) 8937.

[6] (a) U.G.E. Perera, F. Ample, H. Kersell, Y. Zhang, G. Vives, J. Echeverria, M. Grisolia, G. Rapenne, C. Joachim, S.W. Hla, Nat. Nanotechnol. 8 (2013) 46;
(b) G. Vives, H.-P. Jacquot de Rouville, A. Carella, J.-P. Launay, G. Rapenne, Chem. Soc. Rev. 38 (2009) 1551;
(c) G. Vives, A. Carella, J.-P. Launay, G. Rapenne, Coord. Chem. Rev. 252 (2008) 1451;
(d) C. Li, J.C. Medina, G.E.M. Maguire, E. Abel, J.L. Atwood, G.W. Gokel, J. Am. Chem. Soc. 119 (1997) 1609.

[7] (a) D. Lai, F.S.T. Khan, S.P. Rath, Dalton Trans. 47 (2018) 14388;
(b) T. Guchhait, S. Sasmal, F.S.T. Khan, S.P. Rath, Coord. Chem. Rev. 337 (2017) 112;
(c) F.S.T. Khan, T. Guchhait, S. Sasmal, S.P. Rath, Dalton Trans. 46 (2017) 1012;
(d) D. Sil, S.P. Rath, Dalton Trans. 44 (2015) 16195;
(e) F.S.T. Khan, A.K. Pandey, S.P. Rath, J. Chem. Sci. 130 (2018) 85.

[8] (a) A. Kumar, D. Sil, M. Usman, S.P. Rath, Chem. Commun. 55 (2019) 1588;
(b) A.K. Singh, F.S.T. Khan, S.P. Rath, Angew. Chem. Int. Ed. 56 (2017) 8849;
(c) T. Guchhait, S. Sarkar, Y.A. Pandit, S.P. Rath, Chem. Eur J. 23 (2017) 10270;
(d) Y.A. Pandit, S. Sanfui, S.P. Rath, Chem. Eur J. 23 (2017) 13415;
(e) S. Dey, D. Sil, S.P. Rath, Angew. Chem. Int. Ed. 55 (2016) 996;
(f) D. Sil, S. Dey, A. Kumar, S. Bhowmik, S.P. Rath, Chem. Sci. 7 (2016) 1212;
(g) S. Dey, D. Sil, S.P. Rath, Inorg. Chem. 55 (2016) 3229.

[9] (a) F.S.T. Khan, S. Banerjee, D. Kumar, S.P. Rath, Inorg. Chem. 57 (2018) 11498;
(b) F.S.T. Khan, A. Kumar, D. Lai, S.P. Rath, Inorg. Chim. Acta 484 (2019) 503;
(c) S.K. Ghosh, R. Patra, S.P. Rath, Inorg. Chim. Acta 363 (2010) 2791;
(d) S.K. Ghosh, R. Patra, S.P. Rath, Inorg. Chem. 49 (2010) 3449;
(e) S.K. Ghosh, R. Patra, S.P. Rath, Inorg. Chem. 47 (2008) 10196.

[10] P.D. Beer, S.S. Kurek, J. Organomet. Chem. 336 (1987) C17.

[11] S. Stoll, A. Schweiger, J. Magn. Reson. 178 (2006) 42.

[12] SAINT+, 6.02 ed., Bruker AXS, Madison, WI, 1999.

[13] G.M. Sheldrick, SADABS 2.0, University of Göttingen: Göttingen, Germany, 2000.

[14] G.M. Sheldrick, SHELXL-2018: Program for Crystal Structure Refinement, University of Göttingen: Göttingen, Germany, 2018.

[15] M.J. Frisch, G.W. Trucks, H.B. Schlegel, G.E. Scuseria, M.A. Robb, J.R. Cheeseman, G. Scalmani, V. Barone, B. Mennucci, G.A. Petersson, H. Nakatsuji, M. Caricato, X. Li, H.P. Hratchian, A.F. Izmaylov, J. Bloino, G. Zheng, J.L. Sonnenberg, M. Hada, M. Ehara, K. Toyota, R. Fukuda, J. Hasegawa, M. Ishida, T. Nakajima, Y. Honda, O. Kitao, H. Nakai, T. Vreven, J.A. Montgomery Jr., J.E. Peralta, F. Ogliaro, M. Bearpark, J.J. Heyd, E. Brothers, K.N. Kudin, V.N. Staroverov, R. Kobayashi, J. Normand, K. Raghavachari, A. Rendell, J.C. Burant, S.S. Iyengar, J. Tomasi, M. Cossi, N. Rega, J.M. Millam, M. Klene, J.E. Knox, J.B. Cross, V. Bakken, C. Adamo, J. Jaramillo, R. Gomperts, R.E. Stratmann, O. Yazyev, A.J. Austin, R. Cammi, C. Pomelli, J.W. Ochterski, R.L. Martin, K. Morokuma, V.G. Zakrzewski, G.A. Voth, P. Salvador, J.J. Dannenberg, S. Dapprich, A.D. Daniels, Ö. Farkas, J.B. Foresman, J.V. Ortiz, J. Cioslowski, D.J. Fox, Gaussian 09, Revision B.01, Gaussian, Inc., Wallingford, CT, 2010.

[16] (a) A.D. Becke, J. Chem. Phys. 98 (1993) 5648;
(b) C. Lee, W. Yang, R.G. Parr, Phys. Rev. B 37 (1988) 785;
(c) P.J. Stephens, F.J. Devlin, C.F. Chabalowski, M. Frisch, J. Phys. Chem. 98 (1994) 11623.

[17] http://www.chemcraftprog.com.

[18] N.J. Hill, W. Levason, M.C. Popham, G. Reid, M. Webster, Polyhedron 21 (2002) 445.

[19] (a) R. Weiss, A. Gold, J. Terner, Chem. Rev. 106 (2006) 2550;
(b) D. Sakow, D. Baabe, B. Bçker, O. Burghaus, M. Funk, C. Kleeberg, D. Menzel, C. Pietzonka, M. Brçring, Chem. Eur J. 20 (2014) 2913;
(c) Y. Ling, Y. Zhang, J. Am. Chem. Soc. 131 (2009) 6386.

[20] (a) W.R. Scheidt, in: K.M. Kadish, K.M. Smith, R. Guilard (Eds.), The Porphyrin Handbook, vol. 3, Academic Press, New York, 2000, p. 49;
(b) W.R. Scheidt, C.A. Reed, Chem. Rev. 81 (1981) 543.

[21] (a) D. Sahoo, T. Guchhait, S.P. Rath, Eur. J. Inorg. Chem. (2016) 3441;
(b) D. Sahoo, M.G. Quesne, S.P. de Visser, S.P. Rath, Angew. Chem. Int. Ed. 54 (2015) 4796;
(c) D. Sahoo, A.K. Singh, S.P. Rath, Eur. J. Inorg. Chem. (2016) 3305;
(d) D. Sahoo, S.P. Rath, Chem. Commun. 51 (2015) 16790;
(e) R. Patra, S.P. Rath, Inorg. Chem. Commun. (2009) 515;
(f) R. Patra, A. Chaudhary, S.K. Ghosh, S.P. Rath, Inorg. Chem. 47 (2008) 8324;
(g) D. Sahoo, S. Roy, F.S.T. Khan, A.K. Singh, S.P. Rath, Polyhedron (2019), https://doi.org/10.1016/j.poly.2019.02.011.

[22] (a) F.S.T. Khan, S.J. Shah, S. Bhowmik, F.G.C. Reinhard, M.A. Sainna, S.P. Rath, Dalton Trans. 48 (2019), https://doi.org/10.1039/C9DT01182J;
(b) D. Sil, F.S.T. Khan, S.P. Rath, Inorg. Chem. 53 (2014) 11925;
(c) S. Bhowmik, S. Dey, D. Sahoo, S.P. Rath, Chem. Eur J. 19 (2013) 13732;
(d) S. Bhowmik, S.K. Ghosh, S.P. Rath, Chem. Commun. 47 (2011) 4790;
(e) S. Bhowmik, D. Sil, R. Patra, S.P. Rath, J. Chem. Sci. 123 (2011) 827.

[23] (a) F.S.T. Khan, A.K. Pandey, S.P. Rath, Chem. Eur J. 22 (2016) 16124;
(b) D. Sil, F.S.T. Khan, S.P. Rath, Chem. Eur J. 22 (2016) 14585;
(c) D. Sil, A. Kumar, S.P. Rath, Chem. Eur J. 22 (2016) 11214;
(d) M.A. Sainna, D. Sil, D. Sahoo, B. Martin, S.P. Rath, P. Comba, S.P. de Visser, Inorg. Chem. 54 (2015) 1919;
(e) S. Bhowmik, S.K. Ghosh, S. Layek, H.C. Verma, S.P. Rath, Chem. Eur J. 18 (2012) 13025;
(f) S. Bhowmik, S.K. Ghosh, S. Layek, H. C Verma, S.P. Rath, Chem. Eur J. 18 (2012) 13025;
(g) S.K. Ghosh, S.P. Rath, J. Am. Chem. Soc. 132 (2010) 17983.

[24] S. Brahma, S.A. Ikbal, A. Dhamija, S.P. Rath, Inorg. Chem. 53 (2014) 2381.

[25] F.A. Walker, Chem. Rev. 104 (2004) 589;
(b) F.A. Walker, Coord. Chem. Rev. 185–186 (1999) 471.

[26] (a) M. Nakamura, Y. Ohgo, A. Ikezaki, in: K.M. Kadish, K.M. Smith, R. Guilard (Eds.), The Handbook of Porphyrin Science, vol. 7, Word Scientific, Singapore, 2010, p. 1;
(b) A. Ikezaki, Y. Ohgo, M. Nakamura, Coord. Chem. Rev. 253 (2009) 2056;
(c) M. Nakamura, Coord. Chem. Rev. 250 (2006) 2271.

[27] (a) R. Patra, D. Sahoo, S. Dey, D. Sil, S.P. Rath, Inorg. Chem. 51 (2012) 11294;
(b) R. Patra, A. Chaudhary, S.K. Ghosh, S.P. Rath, Inorg. Chem. 49 (2010) 2057;
(c) E.A. Berry, F.A. Walker, J. Biol. Inorg. Chem. 13 (2008) 481;

(d) J. Li, S.M. Nair, B.C. Noll, C.E. Schulz, W.R. Scheidt, Inorg. Chem. 47 (2008) 3841;
(e) T. Teschner, L. Yatsunyk, V. Schünemann, H. Paulsen, H. Winkler, C. Hu, W.R. Scheidt, F.A. Walker, A.X. Trautwein, J. Am. Chem. Soc. 128 (2006) 1379;
(f) L.A. Yatsunyk, A. Dawson, M.D. Carducci, G.S. Nichol, F.A. Walker, Inorg. Chem. 45 (2006) 5417;
(g) C. Hu, B.C. Noll, C.E. Schulz, W.R. Scheidt, Inorg. Chem. 45 (2006) 9721.
[28] S.P. Rath, M.M. Olmstead, A.L. Balch, Inorg. Chem. 45 (2006) 6083.